Research Square

Preprints are preliminary reports that have not undergone peer review.
They should not be considered conclusive, used to inform clinical practice,
or referenced by the media as validated information.

RNA interactions drive structural and functional diversification of α-Synuclein fibrils

Gian Gaetano Tartaglia

gian.tartaglia@iit.it

Istituto Italiano di Tecnologia https://orcid.org/0000-0001-7524-6310

Jakob Rupert

Istituto Italiano di Tecnologia https://orcid.org/0000-0002-0879-1594

Francesco Di Palma

Istituto Italiano di Tecnologia

Alessio Colantoni

Istituto Italiano di Tecnologia

Antonia Intze

Universita' di Roma Sapienza

Maria Eleonora Temperini

Universita' di Roma Sapienza

Valeria Giliberti

Universita' di Roma Sapienza

Elsa Zacco

IIT

Article

Keywords:

Posted Date: April 27th, 2026

DOI: https://doi.org/10.21203/rs.3.rs-9032720/v1

License: This work is licensed under a Creative Commons Attribution 4.0 International License.
Read Full License

Additional Declarations: There is **NO** Competing Interest.

RNA interactions drive structural and functional diversification of α-Synuclein fibrils

Jakob Rupert[1,#], Francesco di Palma[1,2], Alessio Colantoni[1,$], Antonia Intze[3], Maria Eleonora Temperini[3], Valeria Giliberti[3], Elsa Zacco[1,*] and Gian Gaetano Tartaglia[1,*]

1. RNA Systems Biology, Istituto Italiano di Tecnologia, Genoa, Via Enrico Melen, 83, 16152, Genoa, Italy
2. Department of Drug Science and Technology, University of Turin, Via Pietro Giuria, 9, 10125 Turin, Italy
3. Department of Physics, Sapienza University of Rome, Piazzale Aldo Moro 5, 00185 Rome, Italy
4. Center for Life Nano- & Neuroscience, Istituto Italiano di Tecnologia (IIT), Rome, Italy, Viale Regina Elena, 291, 00161 Roma Italy

[#] current affiliation: Institute for Biochemistry, Charité - Universitätsmedizin, Virchowweg 6, 10117 Berlin, Germany

[$] current affiliation: Departmental Faculty of Medicine, UniCamillus-Saint Camillus International University of Health Sciences, 00131 Rome, Italy

* correspondence to: elsa.zacco@iit.it, gian.tartaglia@iit.it

Abstract

RNA has emerged as a modulator of protein aggregation, yet its structural and functional impact on amyloid assemblies remains unclear. Here we show that RNA acts as a cofactor that reshapes the assembly, structure and activity of α-synuclein (aS) fibrils, a central pathological hallmark of Parkinson's disease. Although monomeric aS displays minimal RNA-binding propensity, aggregation confers RNA-binding capacity and enables RNA sequestration. RNA present during fibril formation induces a distinct, more compact cross-β architecture, alters elongation dynamics and suppresses secondary nucleation, generating polymorphs with reduced seeding efficiency in the absence of RNA but RNA-dependent propagation. Functionally, protein-only aS fibrils exhibit catalytic activity that is inhibited by RNA, consistent with RNA–fibril interactions on the fibril surface. By contrast, fibrils templated in the presence of RNA lack detectable catalytic activity, indicating RNA-dependent conformational remodeling of functional sites. RNA also reduces proteolytic degradation of fibrils, consistent with stabilization against clearance mechanisms. Transcriptomic analysis reveals preferential enrichment of uridine-rich RNAs and transcripts encoded by Parkinson's disease–associated genes within RNA–fibril complexes. Together, these findings identify RNA as a structural and functional determinant of aS fibril polymorphism and stability, supporting a model in which nucleic acids contribute to amyloid strain diversification and persistence in synucleinopathies.

Introduction

Alpha-synuclein (aS) is a presynaptic, intrinsically disordered protein implicated in several neurodegenerative disorders, including Parkinson's disease (PD) and multiple system atrophy (MSA) [1]. These conditions are marked by the accumulation of aS into amyloid fibrils, which assemble into intracellular inclusions such as Lewy bodies and glial cytoplasmic inclusions. Traditionally, the toxic gain-of-function in aS pathology has been attributed to fibrillar aggregation. However, recent studies challenge this view. Mahul-Mellier *et al.* demonstrated that fibril presence alone is insufficient to recapitulate disease features, proposing instead that Lewy body formation is a multistep process involving the recruitment of organelles, lipids, and nucleic acids into a structured inclusion—this being the true pathological hallmark [2].

This perspective raises critical questions about the cellular factors modulating aS aggregation. Among these, nucleic acids have emerged as potent modulators of protein assembly. Increasing evidence shows that RNA can influence the kinetics and structure of aggregates formed by proteins such as tau, FUS, and TDP-43 [3,4]. In our previous work, we demonstrated that aggregation confers an acquired RNA-binding ability to aS—a property absent in its monomeric state [5]. We showed that removal of the acidic C-terminal region enhances both aggregation and RNA sequestration, due to favorable electrostatics and increased exposure of the positively charged N-terminus, particularly around residue H50. Although RNA-mediated aggregation of aS is clearly dependent on RNA concentration, the contribution of sequence specificity remains unexplored. It is plausible that certain RNA motifs, such as G-quadruplexes (G4), might play a role in the early stages of aggregation [6].

Previous computational analysis of diverse amyloid-forming proteins revealed a common architecture: hydrophobic, aggregation-prone cores buried within fibrils, flanked by disordered, solvent-exposed regions capable of interacting with nucleic acids [5]. These external domains can contain RNA-binding motifs or electrostatic patches that promote interactions with RNA backbone. For aS, the N-terminal region shows the highest RNA-binding propensity, consistent with cryo-electron microscopy (cryo-) studies of MSA-derived fibrils, identifying unassigned electron densities within positively charged cavities formed by residues K43, K45, and H50 [7].

Building on these observations, this study investigates the functional and structural consequences of RNA binding to aS aggregates. We examined how RNA modulates aggregation kinetics, alters fibril structure, enhances protease resistance, and suppresses the hydrolase activity recently attributed to mature aS fibrils. By estimating RNA-binding affinities and proposing an inhibition model, we reveal a nuanced role for RNA as a cofactor that interacts with fibrils post-aggregation and alters their templated growth. Considering our results alongside previous reports on RNA colocalization with protein aggregates in disease tissue (e.g., tau, hnRNPDL-2 [8]), we propose that RNA contributes actively to the structural and functional diversity of aS aggregates. Understanding the interplay between RNA and aS fibrils may help explain the emergence of disease-specific polymorphs and the selective vulnerability observed in synucleinopathies. It also opens new avenues for RNA-targeted therapeutic interventions in disorders marked by pathological protein aggregation.

Results

RNA alters aS aggregate propagation via seed-specific mechanisms

Previous work indicates that primary nucleation drives aS aggregation under near-physiological conditions [9], and RNA accelerates this process in a concentration-dependent manner [5]. To assess how RNA incorporation during fibril formation influences subsequent propagation, we performed seeded aggregation assays under quiescent conditions. This approach minimizes primary nucleation and allows fibril growth to proceed predominantly through seed elongation and surface-mediated secondary nucleation. We compared the seeding efficiency of fibrils generated in the absence or presence of RNA, hereafter referred to as protein^{only} and protein^{RNA}, respectively. Under these conditions, all reactions displayed exponential fluorescence increases without a detectable lag phase (**Fig. 1A**), consistent with saturated primary nucleation and elongation-dominated growth.

We fit early-phase data (t < 1 h) with a linear model to extract elongation rates (**Supp. Fig. 1A**) Protein^{only} seeds consistently resulted in higher elongation rates than protein^{RNA} seeds (**Fig. 1B**), suggesting that RNA incorporation during fibril formation reduced seeding efficiency. This trend was supported by lower endpoint fluorescence values for proteinRNA seeds (**Supp. Fig. 1B**), indicating reduced total fibril mass. These findings suggested that RNA altered aS aggregate structure and impaired monomer addition.

To further analyze aggregation kinetics, we fit late-stage data (t > 10 h) with a Hill's function (see **Materials and Methods**). At lower seed concentrations, protein^{only} seeds in the absence of RNA showed a higher Hill's coefficient (h = 1.77 ± 0.67) than those with RNA (h = 1.12 ± 0.31), consistent with more prominent secondary processes (**Supp. Fig 2A)**. Thus, fibril growth under these conditions is driven by elongation and secondary nucleation and RNA appears to accelerate elongation while reducing surface-mediated secondary nucleation (**Fig. 2A**). In contrast, protein^{RNA} seeds show minimal changes in aggregation rate in the absence of RNA even at higher seed concentration. The addition of RNA results in notably higher aggregation rates which also scale linearly with seed concentration. (**Fig. 2B**). This suggests that RNA is required for efficient propagation of protein^{RNA} fibrils. Consistent with previous observations that aS sequesters RNA during aggregation [5], we detected lower soluble RNA levels after aggregation with protein^{RNA} seeds compared to protein^{only} seeds ($p < 0.001$, N = 8, **Supp. Fig. 2B**). This supports a model in which co-aggregation enhances fibril RNA-binding capacity and promotes RNA-templated propagation.

Together, these findings identify RNA as an active cofactor that reshapes the structure and propagation of aS aggregates.

RNA changes the structural properties of aS aggregates

To assess the impact of RNA on the structure of protein^{RNA} and protein^{only} seeded fibrils, we used Fourier-Transform Infrared (FTIR) spectroscopy [10]. Spectra recorded from mm^2-sized areas of sample deposited on CaF_2 substrate revealed a strong β-sheet peak around 1630 cm^{-1} (hereafter cross-β peak) in the amide I region (1600 – 1700 cm^{-1}) (**Fig. 3A, top**), characteristic of amyloid structures [11]. In protein^{RNA} fibrils, this peak was shifted to lower central frequencies ($\omega_{cross\text{-}\beta}$), as confirmed by second derivative analysis (**Fig. 3A, bottom**), suggesting a more compact fibrillar structure with stronger hydrogen bonding[12].

Because spectra acquired from larger sample areas may average over diverse fibril conformations, we repeated the analysis using FTIR microspectroscopy (micro-FTIR) with a focal plane array (FPA) detector. This setup enabled spectral acquisition from 2.7 x 2.7 μm^2 regions across a 64 x 64 pixel array and statistical analysis of $\omega_{cross\text{-}\beta}$ frequencies at higher spatial resolution (**Fig. 3B**). Both protein^{only} and protein^{RNA} fibrils displayed a bimodal $\omega_{cross\text{-}\beta}$ distribution, indicating two main distinct polymorphs. The more compact polymorph ($\omega_{cross\text{-}\beta} \approx 1625.8$ cm^{-1}) was significantly enriched in protein^{RNA} fibrils, while protein^{only} fibrils showed a broader distribution.

Consistent with these observations, atomic force microscopy (AFM) imaging revealed morphological differences between fibril types (**Fig. 3C**). Protein^{only} fibrils appeared relatively uniform and slightly curved, while protein^{RNA} fibrils were shorter, more heterogeneous, and prone to clustering. These findings demonstrate that RNA promotes the formation of more compact aS fibril polymorphs with distinct supramolecular organization.

RNA binding to aS fibril inhibits proteinase K digestion

We then assessed whether the increased structural compactness of RNA-induced aS fibrils reduces proteolytic degradation, a key mechanism in aggregate clearance [13]. Because proteolysis requires access to the fibril surface, we also asked whether RNA binding could directly impede proteinase K (pK) activity.

Fibrils grown from protein^{only} seeds were incubated with pK and increasing RNA concentrations and analyzed by SDS-PAGE (**Supp. Fig. 3A**). To quantify this effect, we added pK directly to aggregation assay wells at reaction endpoint and monitored Proteostat^{TM} fluorescence, assuming successful digestion would lead to a fluorescence decrease upon fibril degradation. Indeed, increasing RNA concentrations slowed the fluorescence decay (**Fig. 4A**) and kinetics fits revealed an exponential decrease in initial reaction velocity (**Supp. Fig. 3B**). RNA did not inhibit pK activity towards a soluble substrate (pNPA) in the absence of aS fibrils (**Supp. Fig. 3C**), indicating that RNA inhibits proteolysis by shielding the fibril surface rather than inhibiting the enzyme.

We next asked whether removing RNA could restore proteolytic efficiency. Fibrils grown from protein^{only} or protein^{RNA} seeds in the presence or absence of RNA were treated with RNase A prior to pK addition. RNase A alone had no effect on fluorescence (**Supp. Fig. 3D**). For fibrils grown without RNA, RNase A did not alter degradation rates (**Fig. 4B**). In contrast, protein^{only} fibrils grown with RNA were degraded significantly faster following RNase A treatment (**Fig. 4B**), confirming that surface-bound RNA impedes proteolysis. Protein^{RNA} fibrils grown with RNA showed no significant change after RNase A treatment ($p = 0.06$, $N = 11$) and displayed a rapid initial fluorescence decrease followed by a pronounced slowdown. This suggests that RNA is sequestered within protein^{RNA} fibrils and becomes exposed during early digestion, subsequently inhibiting further degradation (**Supp. Fig. 3D**).

These findings indicate that RNA binding to aS fibrils impairs proteolytic clearance and that the mode of RNA association depends on fibril growth history (**Fig. 4C**).

RNA interacts directly with aS fibrils and inhibits their catalytic activity

Having shown that RNA inhibits proteinase K digestion of aS fibrils, we next tested whether this effect results from direct RNA binding to the fibril surface. To this end, we leveraged the recently described catalytic hydrolase activity of aS fibrils [14]. Fibril enzymatic activity has been linked to the sole histidine, H50, located within a region predicted to have high RNA-binding propensity as predicted by *cat*RAPID [15,16](**Supp. Fig. 4**). In the "rod 1a" polymorph [17] this region forms a pocket around H50 that resembles an RNA-binding pocket in RNA-induced tau fibrils (**Fig. 5A**)[4].

We hypothesized that RNA binding would inhibit catalytic activity and thereby provide a functional readout of RNA–fibril interaction. After validating the catalytic activity of protein^{only} aS fibrils (**Supp. Fig. 5, Supp. Table. 1**), we measured hydrolysis of two substrates—para-nitrophenyl acetate (pNPA) and para-nitrophenyl phosphate (pNPP)—in the presence of increasing RNA concentrations. RNA markedly reduced activity towards both substrates (**Fig. 5B**). Fitting the inhibition curves with a four-parameter logistic model [18] yielded apparent $K_{0,5}$ values of 680 ng/µL (pNPA) and 602 ng/µL (pNPP), corresponding to an estimated affinity of 7 µM for total yeast RNA.

The data cannot provide the exact inhibition mechanism, however analysis likely reveals a number of binding spots for RNA molecules with different affinities (**Supp. Fig. 6**). In contrast, fibrils grown from protein^{RNA} seeds in the absence of RNA displayed no detectable enzymatic activity, with hydrolysis rates indistinguishable from baseline for both substrates (**Fig. 5C**). This indicates that structural changes induced by RNA co-aggregation impair catalytic function, likely by restricting access to residues such as H50. Similarly, fibrils formed in the presence of heparin also lacked catalytic activity (**Fig. 5C**).

aS fibrils preferentially sequester uridine-rich RNA

To identify RNA species that interact with aS fibrils, we performed RNA sequencing on RNA recovered from fibril–RNA complexes. Total RNA from HEK293T cells was used to enable efficient library preparation. We compared two experimental conditions: (i) RNA present during fibril formation (*coaggregation*), in which RNA becomes incorporated into protein^{RNA} fibrils, and (ii) RNA incubated with preformed protein^{only} fibrils (*RNA pull-down*), which captures RNAs that bind mature fibrils. RNA-only samples were included as controls for differential enrichment analysis (see **Materials and Methods**).

Hexanucleotide motif analysis revealed distinct binding preferences between fibril types. Protein^{RNA} fibrils showed strong enrichment for AU-rich motifs, particularly uridine, after normalizing for transcript abundance (**Fig. 6A**) and length (**Supp. Fig. 7**), whereas GC-rich motifs were depleted. To place these findings in a structural context, we examined disease-associated aS fibril structures. CryoEM structures from multiple system atrophy (MSA) brains contain unassigned electron densities closely associated with the fibrils (PDB 6XYP and 6XYO [7]), forming a hydrophilic cavity in proximity to residues such as Lys43, Lys45 and His50.

Using the 6XYP structure, we conducted molecular docking of individual ribonucleotides and deoxynucleotides into this cavity (**Fig. 6C-E;** see **Materials and Methods**). Pyrimidine nucleotides, particularly uridine,were preferentially accommodated within the planar pose of the filament, whereas purines showed less favorable binding due to steric constraints. Docking scores further favored

ribonucleotides over deoxynucleotides, consistent with the electrostatic environment of the cavity and the presence of hydrogen-bonding residues. These results align with our previous observation that aS sequesters DNA less efficiently than RNA (**Fig. 6B-E**)[5].

Together, these data suggest that nucleic acids can occupy the unidentified electron-dense cavities observed in patient-derived aS fibrils and provide a structural basis for the preferential sequestration of uridine-rich RNA.

aS fibrils significantly sequester PD related transcripts

Using a high-stringency PD trait definition from the EBI GWAS Catalog (MONDO_0005180)[19], we assessed whether transcripts enriched in the RNA-aS co-aggregation set were associated with PD genetic risk. Here, *coaggregated transcripts* refer to RNAs significantly enriched in fibrils formed in the presence of RNA relative to matched pull-down controls (1,034 genes; see **Materials and Methods).** This coaggregated gene set showed robust overrepresentation of PD-associated loci compared with a background of 25,739 protein-coding genes (odds ratio = 2.73, p = 0.0060; Fisher's exact test, **Materials and Methods; Supp. Table 2**). In contrast, control gene sets matched for transcript length or abundance (1,018 and 1,007 genes, respectively) exhibited no significant association with PD genetic risk (length-matched OR = 1.59, p ≈ 0.29; abundance-matched OR = 0.51, p ≈ 0.60; Fisher's exact test). These results indicate that the observed enrichment is not attributable to transcript length, abundance, or sampling bias. Among the PD-associated loci represented in the coaggregation set are genes linked to lysosomal, mitochondrial, and vesicular pathways, including GALC, GCH1, SH3GL2, WDR41, CRLS1, and PAM. These genes have been independently implicated in PD-related cellular processes such as lysosomal function, dopamine metabolism, synaptic vesicle recycling, autophagy, mitochondrial phospholipid remodeling and neuromodulator processing [20–25] . Their presence in the fibril-associated transcriptome suggests that RNA species interacting with aS fibrils may be non-randomly drawn from pathways previously connected to α-synuclein biology.

In addition to GWAS-identified loci, the coaggregation set includes transcripts corresponding to genes with established experimental or clinical links to PD, including FBXO7, UCHL1, and HMOX1[26–30]. While these genes are not all captured by population-level association studies, they are implicated in pathways relevant to proteostasis, mitochondrial function, and redox regulation. Together, these observations suggest that RNA–aS coaggregation may intersect with molecular pathways relevant to PD, although the functional and pathological significance of this association remains to be determined.

Discussion

Our study uncovers a multifaceted role for RNA in modulating the aggregation, propagation, and structural diversification of aS fibrils. Building upon prior findings implicating nucleic acids as cofactors in amyloidogenesis [31,32], we show that RNA not only influences the kinetics of aS aggregation but also the structural and functional properties of the resulting amyloid assemblies. This work refines the emerging paradigm that amyloid fibrils are not purely proteinaceous but can co-assemble with endogenous molecules—particularly RNA—generating distinct, functionally diverse polymorphs.

Extending our previous observations that RNA accelerates the *de novo* aggregation of aS [5], we demonstrate here that RNA co-aggregation alters aS seeding efficacy in a concentration- and seed-dependent manner. Under seed-saturating, quiescent conditions that minimize mechanical fragmentation, protein^{only} seeds grow faster than their RNA-containing counterparts, suggesting that RNA incorporation induces fibril conformations that sterically limit monomer addition.

Adding RNA to protein^{only} seeds reveals a dual effect: It enhances elongation at high seed concentrations (5–10 μM) but suppresses fibril growth at lower concentrations. RNA also modifies the kinetic pathway by promoting elongation and suppressing secondary nucleation, a process known to dominate physiological aggregation and contribute to toxic oligomer formation [33] [34] Conversely, RNA enables efficient elongation of protein^{RNA} seeds with kinetics on par with protein^{only} seeds, supporting the notion that RNA-induced fibrils adopt distinct conformations that require continued cofactor interaction—a phenomenon observed for tau and MSA-associated fibrils [4,7]. This behavior hints at a conformational gating mechanism or competitive binding equilibrium, in which interactions between monomeric aS and fibril-bound RNA may facilitate or restrict templated fibril elongation [35,36].

Spectroscopic and morphological analyses reveal that RNA co-aggregation favors the formation of more compact and rigid fibrils. Shifts in cross-β peaks (FTIR) and distinct AFM height profiles show reduced heterogeneity compared to protein^{only} fibrils, a feature previously linked to altered seeding potency and cellular toxicity [9,32]. RNA may also confer partial resistance to proteolytic degradation: while RNase-treatment rescues the slowed proteinase K degradation of protein^{only} fibrils, protein^{RNA} fibrils remain more resistant, suggesting that RNA interactions could limit cellular clearance. Positively charged amino acids on the fibril surface may further impede ubiquitination or chaperone recognition [37], potentially allowing RNA-bound aggregates to persist longer in cells.

A key finding is the direct interaction between RNA and aS fibrils, revealed through inhibition of fibril catalytic activity centered around H50. Estimated RNA-binding affinity are two orders of magnitude lower than monomer-fibril interactions [34], supporting potential physiological relevance. In RNA- or heparin-induced fibrils, catalytic activity is lost, indicating that the chemical environment around H50 is altered. This is noteworthy as H50 is buried in the fibril core of patient-derived aS amyloids from Lewy-body dementia and MSA [7,38]. These results suggest that RNA may influence the formation of disease-relevant fibril conformations. Structural modeling further indicates that pyrimidine nucleotides engage hydrophilic pockets and positively charged residues (including H50) in patient-derived MSA fibrils. Electrostatic

complementarity appears to drive selective RNA binding, which is supported by RNA sequencing showing enrichment of uridine-rich motifs in protein^{RNA} fibrils. Interestingly, our data suggest a functional distinction between RNA species: structured, G-rich RNAs may transiently promote aggregation initiation, while AU-rich, uridine-containing RNAs are stably sequestered within elongating fibrils. This two-stage model reflects temporally distinct roles for RNA in modulating aggregation kinetics and structural evolution. Although our experiments were conducted in non-neuronal cells, a disease-related trend is evident: transcripts retained in protein^{RNA} fibrils encode proteins converging on lysosomal, mitochondrial, and synaptic–vesicular pathways implicated in PD. Notable examples include GALC (lysosomal function), GCH1 (dopamine synthesis) [21], SH3GL2 (synaptic vesicle recycling) [22], WDR41 (autophagic and lysosomal regulation) [23], and CRLS1 (mitochondrial phospholipid remodeling) [24]. While these associations are correlative, they suggest that RNA–protein coaggregation may preferentially capture transcripts from pathways relevant to PD-related cellular processes

In conclusion, RNA acts as a dynamic cofactor in aS aggregation, shaping the structural, kinetic, and functional properties of fibrils. RNA may influence the formation or propagation of distinct amyloid strains, adding a layer of complexity to strain heterogeneity. Our findings open avenues for therapeutic strategies targeting RNA-fibril interactions to destabilize pathogenic polymorphs or enhance aggregate clearance. Further investigation is needed to define RNA identity, binding motifs, and phase-separated environments to fully elucidate RNA's role in synucleinopathies.

Materials and Methods

Preparation of alpha-synuclein seeds

Expression and purification of recombinant aS was performed as described previously [5]. Seeds were prepared by aggregating 100 µM aS in the presence or absence of 500 ng/µL total yeast RNA (totRNA, Roche, cat. no. 10109223001) in black, clear-bottom 96-well plates (VWR, cat. no. VWRI732-3738) containing a 3-mm borosilicate glass bead. Aggregation was carried out at 37 °C with constant shaking in a Spark microplate reader (Tecan) for 24 h. Samples were transferred into Protein LoBind tubes (Eppendorf, cat. no. 0030108116) and centrifuged at 18,000 g for 1 h at room temperature. Supernatants were removed, and soluble protein concentration was determined using a bicinchoninic acid assay (BCA) assay (Thermo Fisher Scientific, cat. no. 23225) or Qubit Protein assay (Thermo Fisher Scientific, cat. no. Q33212). Seed concentration was calculated by subtracting the soluble protein concentration from the initial protein concentration. Pelleted aggregates were resuspended in sterile PBS and centrifuged again at 18,000 g for 1 h at room temperature. After removal of the supernatant, pellets were resuspended in sterile PBS, and RNase A (Thermo Fisher Scientific, cat. no. EN0531) was added to a final concentration of 50 µg/mL to degrade sequestered RNA. Samples were incubated at 37 °C for 1 h, followed by addition of 1 U/mL RiboLock RNase inhibitor (Thermo Fisher Scientific, cat. no. EO0381) . Samples were centrifuged at 18,000 g for 30 min at room temperature, the supernatant was discarded, and the washing step was repeated twice. The final pellet was resuspended in sterile PBS, aliquoted into Protein LoBind tubes, flash-frozen, and stored at -80 °C.

Seeded aggregation assays

A fresh aS aliquote was rapidly thawed and filtered through a 0.22 µm syringe filter (Merck - Sigma Aldrich, cat. no. SLGVR04). Total yeast RNA (Roche, cat. no. 10109223001) was resuspended in aggregation buffer (20 mM potassium phosphate pH 7.2, 100 mM KCl, 5 mM $MgCl_2$), and its concentration was measured using NanoDrop spectrophotometer (Thermo Fisher Scientific, cat. no. ND-ONE-W). Seed aliquots were rapidly thawed and sonicated in a water bath sonicator for 10 min at room temperature. All reagents were mixed in Protein LoBind tubes, and Proteostat™ (Enzo Life Science, cat. no. ENZ-51023-KP002) was added as a fluorescent aggregation marker. Final concentrations were 50 µM monomeric aS and 500 ng/µL for totRNA in aggregation buffer, with seed concentrations ranging from 1 to 10 µm. Aliquots (100 µL) were transferred to wells to black, clear-bottom 96-well plates (VWR, cat. no. VWRI732-3738), sealed and incubated at 37 °C without agitation until fluorescence reached a plateau (ca. 40 h). Proteostat™ fluorescence was recorded from the bottom of the wells every 15 min, and each condition (e.g. seed concentration) was measured in at least four replicates.

Analysis of aggregation assay data

As fluorescence data was recorded at 5 different points per well, signals were first averaged at all timepoints. Background fluorescence (buffer or buffer/RNA) was subtracted, and fluorescent traces were normalized according to minimum and maximum well fluorescence value. Data recorded at $t < 1$ h were fitted with a linear trendline, and the slope was determined for each replicate. Slops were then averaged for each condition and reported as the aggregation rate.

To determine the fluorescence trace curvature, data points at t > 10 h were fitted to a sigmoid equation as described previously [5]. The coefficient *h* was calculated from individual fits and averaged across conditions, and was used as a measure of curve curvature, indicating the presence of secondary processes.

Proteinase K fibril degradation assay

Fibrils were prepared as described for the enzyme catalysis reactions (see below). Following centrifugation, supernatants were discarded and pelleted aggregates were resuspended in PBS containing 0.5 µg/mL proteinase K (pK; Roche, cat. no. 3115887001). Samples were incubated at 37 °C with mild agitation for 5 h. Reactions were stopped by addition of 6x SDS-PAGE loading dye, and samples were boiled at 95 °C for 10 min before separation on a 4-12 % denaturing polyacrylamide gel (Invitrogen, cat. no. NP0321). Gels were stained with InstaBlue (Expedeon, cat. no. ISB1L).

Fluorescence fibril degradation assays

After fluorescence reached plateau for all conditions, the microplate containing aggregated aS was briefly removed from the plate reader. For each condition, half of the wells were used as controls by adding 2 µL PBS, while the remaining wells were treated with RNase A by addition of 2 µL RNase A stock (Thermo Fisher Scientific, cat. no. EN0531) in PBS. The plate was immediately resealed and returned to the microplate reader set to 37 °C. Fluorescence was recorded from the bottom of the wells every 5 min, with 10 s of shaking before each measurement, for 5 h. The plate was then removed, and 2 µL of proteinase K (Roche, cat. no. 3115887001) solution (2.5 mg/mL in PBS; final concentration 0.5 µg/mL) was added to each well. The plate was immediately resealed and returned to the microplate reader set to 37 °C and fluorescence was measured every 5 min with 10 s shaking before each measurement for a further 20 h.

Analysis of fibril degradation assays

Fluorescence signals were recorded at 5 positions per well and averaged at all time points. Background fluorescence (buffer or buffe with RNA) was subtracted and fluorescence traces were normalized to the minimum and maximum well fluorescence signal.

Traces were linearised and fitted to the model function (1):

(1) $ln(\frac{F(x)-A}{B}) = kx$

where *A* and *B* are fitting parameters. The parameter *k,* corresponding to the slope of the initial linear region of the fluorescence decay, was used as a measure of the initial reaction rates. Initial rates for each condition were averaged and compared using a two-way paired Student *t*-test.

Fibril enzymatic activity assay

Fibril enzymatic activity assays were performed as described previously [14]. Fibrils were prepared by mixing 200 µM monomeric aS with 5 µM seeds, prepared as described above, in aggregation buffer in Protein LoBind tubes. Heparin-seeded fibrils were prepared using the same protocol, with total yeast RNA replaced by heparin (Merck - Sigma Aldrich, cat. no. H3149). Fibrils were grown at 37 °C without agitation

for 5 days and were prepared fresh on the day of the enzymatic assay. Samples were centrifuged at 18,000 g for 1 h at room temperature, and the protein concentration of the supernatant was determined using a BCA assay. Fibril concentrations were calculated by subtracting the supernatant concentration from the initial monomer concentration (200 µM). Pellets were resuspended in sterile PBS to a monomer-equivalent concentration of 200 µM. Reaction mixtures were prepared in Protein LoBind tubes by combining sterile PBS, 0.5 M $MgCl_2$, and freshly resuspended total yeast RNA. Fibrils were sonicated in a water bath sonicator for 15 min at room temperature (setting 8) and added to the reaction mixtures. To promote fibril-RNA interactions, mixtures were incubated at room temperature with gentle mixing for 30 min. Substrate was then added to a final concentration of 10 mM p-nitrophenyl phosphate (pNPP, Merck - Sigma Aldrich cat. no. 71768) or 5 mM p-nitrophenyl acetate (pNPA, Merck - Sigma Aldrich cat. no. N8130). Reactions were briefly mixed, aliquoted into transparent 96-well plates (Costar cat. no. 3370), sealed, and incubated at 37 °C for up to 16 h. Enzymatic activity was followed by measuring absorbance at 410 nm (A_{410}) every 3 min in a Spark microplate reader (Tecan).

Analysis of enzymatic activity assays

Time-resolved A_{410} data were first blanked by subtracting A_{410} values from wells containing substrate and buffer only, eliminating any background catalytic activity or substrate auto-hydrolysis. A_{410} values were then converted to the molar concentrations of 4-nitrophenol (pNP) using its extinction coefficient (ε = 7500 $M^{-1}cm^{-1}$ in 50 mM phosphate buffer, pH 7).

Basic kinetic parameters (K_M, k_{cat}, ε) were determined as outlined by Horvath *at al.* [14]. RNA binding affinities were estimated by plotting fitted initial velocities (v_0) at varying RNA concentrations against the corresponding RNA concentration. Data were fitted using a four-parameter logistic equation (2):

$$(2)\ v_i = v_o - \frac{(v_o - v_\infty)\cdot[S]^h}{K_{0.5}^h + [S]^h}$$

v_0, v_∞, $K_{0.5}$ and h are fitting parameters, and [S] is the initial substrate concentration.

FTIR measurements

For IR experiments, 20 µL sample were deposited at the center of CaF_2 windows and allowed to dry completely under a gentle nitrogen flow in low-humidity conditions. FTIR spectra were recorded using a Bruker VERTEX 70v spectrometer (Bruker Optic GmbH, Ettlingen, Germany) equipped with a N_2-cooled mercury-cadmium-telluride (MCT) detector (Infrared Associates Inc., United States). The interferometer was operated under low vacuum to minimize IR absorption of atmospheric CO_2 and water vapor. Spectra were acquired from 1200 to 6000 cm^{-1} with a 2 cm^{-1} resolution and 512 scans.

Micro-FTIR measurements

Micro-FTIR spectra were acquired using a Vertex 80 spectrometer (Bruker Optic GmbH, Ettlingen, Germany) coupled to a Hyperion 3000 IR-microscope (Bruker Optic GmbH, Ettlingen, Germany) at the IRIS beamline at BESSY II, Helmholtz Zentrum Berlin. The Hyperion 3000, continuously purged with nitrogen, was equipped with a 15x Cassegrain objective lens (numerical aperture, NA = 0.4). Data were acquired using a liquid-nitrogen cooled 64 x 64 pixel focal plane array (FPA) detector, covering a 173 x 173 $µm^2$ area

(single pixel area is 2.7 x 2.7 μm^2). Spectra were recorded in transmission mode using the internal Globar source over 800-4000 cm^{-1}, with 2 cm^{-1} resolution of and 64 scans.

Analysis of IR spectra

FTIR spectra were baseline-corrected, spline-smoothed, and normalized in IgorPro 6.22A, which was also used to compute second-order derivatives. For micro-FTIR $\omega_{cross-\beta}$ analysis of protein^{only} and protein^{RNA} fibrils (FPA detector), spectra (64 × 64 per acquisition) were baseline-corrected over 1480–1730 cm^{-1} and integrated over 1490–1720 cm^{-1} to generate amide-I/II intensity maps in OPUS 8.7. Second-order derivatives were calculated using the Savitzky–Golay method (9-point smoothing), and an $\omega_{cross-\beta}$ maps were generated by identifying derivative minima within 1624–1632 cm^{-1} using the *peak-picking* function in OPUS. Spectra lacking a single minimum in this range were excluded due to low signal-to-noise ratio. To remove pixels with low protein content, an intensity mask (50–100% of maximal amide-I/II signal) was generated in the amide-I/II map in Gwyddion 2.61 and applied to the $\omega_{cross-\beta}$ map. The masked pixels were then used to generate the histograms of the $\omega_{cross-\beta}$ distribution in IgorPro 6.22A.

AFM topographic map

Three aliquots of 2 µL of protein^{only} seeds and protein^{RNA} seed samples were drop-cast onto 1 cm x 1 cm template-stripped gold surfaces (Platypus Technologies, 0.3 nm nominal roughness) for 5 min, then rinsed with 40 µL Milli-Q water to achieve a sparse distribution. Samples were allowed to dry for 1 h under a gentle nitrogen flow in a controlled low-humidity environment. AFM topographies were recorded using the AFM module of the neaSNOM system (attocube systems AG, Germany) at the IRIS beamline at BESSY II, Helmholtz Zentrum Berlin. Protein^{only} seeds were imaged with an Arrow-NCPt (tip radius <25 nm) Pt/Ir-coated AFM probe (Nanoworld AG, Switzerland), while protein^{RNA} seeds were imaged with a PPP-NCSTAu (tip radius <50 nm) Au-coated AFM probe (Nanosensors, Switzerland). Measurements were performed in tapping mode at room temperature.

RNA extraction from aS aggregates

RNA was extracted from HEK293T cells grown under standard culture conditions using the Direct-Zol RNA Mini-Prep kit (Zymo Research #R2050), including DNase treatment before the final purification step. Total cell RNA was eluted in nuclease-free water. Monomeric aS (50 µM) was aggregated in aggregation buffer in the presence or absence of 500 ng/µL total cell RNA in 1.5 mL DNA LoBind tubes (Eppendorf) at 37 °C with constant agitation for 72 h. Aggregation buffer containing 500 ng/µL total cell RNA was included as a control. Samples were centrifuged at 18,000 g for 1 h at 4 °C. For protein^{RNA} fibrils, supernatants were removed and preserved as the "non-sequestered fraction". For the protein^{only} fibrils, supernatants were removed and pellets were resuspended in the same volume of aggregation buffer containing 500 ng/µL total cell RNA ("RNA pull-down") followed by gentle agitation at room temperature for 2 h. Control samples containing 500 ng/µL total cell RNA in buffer were included. Samples were centrifuged again at 18,000 g for 1 h at 4 °C, and supernatants were collected as the "non-sequestered" fraction. Pellets were washed twice with the same volume of aggregation buffer at 4 °C, then gently resuspended in aggregation buffer and centrifuged for a final 1 h at 18,000 g at 4 °C. RNA was extracted from the pellets as described previously [5].

Experiments were repeated three times independently, with four replicates per condition (coaggregation and pull-down). RNA quality was assessed using a BioAnalyzer, and three replicates per experiment were selected for library preparation.

RNA sequencing experiment and analysis

Next-generation sequencing libraries were prepared using the Illumina Total RNA Prep with Ribo-Zero Plus kit and sequenced on a Illumina NovaSeq 6000. BCL-to-FASTQ conversion, demultiplexing, adapter trimming, and removal of reads shorter than 35 nucleotides were performed using bcl2fastq (v2.20). Reads mapping to human rRNA were removed with Bowtie2 (version 2.3.4.1) [39], and remaining reads were aligned to the human genome (hg38) using STAR (version 2.7.6a) [40], with GENCODE release 43 GTF annotation. Alignment parameters were: *--quantMode GeneCounts --outSAMstrandField intronMotif --outSAMtype BAM SortedByCoordinate --readFilesCommand zcat --peOverlapNbasesMin 10*. Resulting BAM files were merged with SAMtools (version 1.7) [41] and used for transcriptome assembly with StringTie (version 2.2.1) [42] (*--rf,* GENCODE GTF reference). Post-assembly, transcripts assigned to known genes were retained while rRNA annotations were excluded. Transcripts were prioritized by FPKM and genomic uniqueness. Transcripts were excluded if their unique regions were <50 bp or their FPKM <10% of the top isoform. Gene coordinates were updated to reflect retained transcripts, generating a reduced GTF file. Multi-exon coordinates were written to a BED file, and precursor transcript sequences were extracted using BEDTools getfasta [43] and GffRead [44]. These sequences were combined to generate a reference transcriptome. Transcript abundances were quantified using Salmon (version 1.3.0) [45] with parameters *-l ISR --gcBias --numBootstraps 30 –validateMappings*. Salmon output was converted for sleuth analysis using prepare_fish_for_sleuth function (wasabi v1.0.1), and transcript level abundances were imported into R (v3.6.3) using tximport (v.1.18.0) [46]. Differential transcript abundance analyses were performed with sleuth (v.0.30.0) [47], considering transcripts with average FPKM > 0.1. Wald tests (sleuth_wt) identified transcripts enriched in the protein^{RNA} or protein^{only} fibrils relative to RNA pull-down controls (q-value < 0.05, $\log_2$ fold-change ≥ 0.58). Likelihood ratio tests (sleuth_lrt) were used to identify transcripts with differential enrichment between protein^{RNA} and protein^{only} fibrils. Protein^{RNA}-enriched transcripts were defined as those with LRT q-value < 0.05 and a fibril/control ratio at least 1.5 times higher than in the protein^{only} experiment.

To assess 6-er enrichment, protein^{RNA}-enriched transcripts were compared against two control sets: abundance-matched and length-matched transcripts with LRT q-value > 0.25. Only non-precursor molecules were included. Chi-square tests were performed for each 6-mer to compare proportional representation between protein^{RNA}-enriched transcripts and controls. P-values were adjusted for multiple testing using the Benjamini-Hochberg correction.

RNA and DNA computational docking

Deoxyribo- and ribonucleotides monophosphate used as ligand molecules were retrieved from the PDB (http://RCSB.org) and imported in Maestro (*Schrödinger Release 2023-2: Maestro*; Schrödinger LLC: New York, NY, USA, 2023). Ligand preparation was performed using LigPrep, assigning the prevalent protonation and tautomeric states. Protein models of aS fibril were prepared with the Protein Preparation Wizard and trimmed from the PDB ID 6XYP structure [7] to include one or two protein dimers. Hydrogen

assignment was based on hydrogen-bond network optimization. The docking grid was centered at the centroid of Lys43, Lys45 and His50 of each aS chain in the single or the double dimer, with box size accommodating ligands up to 20 Å. Docking followed a three-step Glide protocol: SP, XP, and IF. In SP docking, ligand conformations were generated via extensive conformational search, filtered for spatial compatibility, minimized the target using the OPLS3 force field [48], and optimized using Monte Carlo simulations. Poses were ranked using the default GlideScore [49]. XP docking employed an anchor-and-grow sampling approach with a stricter scoring function [50]. IF docking included van der Waals radii reduction and increases non-bonded interactions cut-offs. To improve ligand accommodation, the Prime module predicted and re-oriented side chains of surrounding residues. Ligands and residues were minimized, and ligands were re-docked [51,52]. Five docking poses were generated per ligand and ranked by GlideScore, with the top pose for each nucleotide considered for comparative analysis.

PD GWAS coaggregation Enrichment Analysis

Transcripts significantly enriched in fibril versus control conditions (sleuth_wt, $q < 0.05$) were designated as coaggregated RNAs while two independent matched control sets—length-matched and abundance-matched transcripts ($q > 0.25$)—were constructed to account for sequence composition and expression level. PD GWAS data were obtained from the NHGRI-EBI Catalog (MONDO_0005180; downloaded November 2025) [19]. Variants with $P \leq 1\times10^{-7}$ were grouped by REGION, and gene names extracted from MAPPED_GENE, REPORTED GENE(S), and SNP_GENE_SYMBOLS were standardized, deduplicated, and filtered by requiring at least two independent annotations per locus. Genes were intersected with a fixed universe of 25,739 human genes and capped at two genes per region, yielding a high-confidence PD GWAS set of 98 genes. Enrichment of co-aggregated RNAs in PD risk genes was evaluated using Fisher's exact test against a competitive background.

Data availability

The RNA-seq data generated in this study have been deposited in the Gene Expression Omnibus (GEO) under accession number GSE311054. The following secure token can be used by reviewers to access the GEO record while it remains in private status: yxkvckkoxtyvxub.

Acknowledgments

The authors would like to thank the RNA flagship at IIT, Istvan Horvath and Pernilla Wittung Stafshede for helpful discussions and insights. AI, MET, and VG would like to thank Helmholtz-Zentrum Berlin für Materialien und Energie for the micro-FTIR and AFM measurements carried out at the IRIS beamline of BESSY II.

Funding

The research leading to these results have been supported through ERC [ASTRA_855923 (to G.G.T.), H2020 Projects IASIS_727658 and INFORE_825080 and IVBM4PAP_101098989 (to G.G.T.)] and National Center for Gene Therapy and Drug based on RNA Technology (CN00000041), financed by NextGenerationEU PNRR MUR - M4C2 - Action 1.4- Call “Potenziamento strutture di ricerca e di campioni nazionali di R&S” (CUP J33C22001130001) (to G.G.T.). Funding for open access charge: ERC ASTRA_855923 (to G.G.T.). F.D.P. acknowledges the support granted by the European Union - Next Generation EU, Mission 4 Component 1 CUP D53D23016360001, PRIN-PNRR, Grant n. P2022CLXMK, for his current position at the DSTF, UniTo.

Contributions

GGT and JR conceived the study. JR performed all biochemical experiments. EZ, GGT, and JR wrote the manuscript. GGT and EZ supervised JR. AC analyzed the transcriptomic data, and FDP ran the dockings and analyzed them to generate the structural models. VG, MET, and AI performed the infrared spectroscopy experiments and analyzed infrared data with JR. All authors discussed the results, provided critical feedback, and approved the final manuscript.

References

1. Calabresi, P. *et al.* Alpha-synuclein in Parkinson's disease and other synucleinopathies: from overt neurodegeneration back to early synaptic dysfunction. *Cell Death Dis.* **14**, 176 (2023).
2. Mahul-Mellier, A.-L. *et al.* The process of Lewy body formation, rather than simply α-synuclein fibrillization, is one of the major drivers of neurodegeneration. *Proc. Natl. Acad. Sci. U. S. A.* **117**, 4971–4982 (2020).
3. Zacco, E. *et al.* RNA as a key factor in driving or preventing self-assembly of the TAR DNA-binding protein 43. *J. Mol. Biol.* **431**, 1671–1688 (2019).
4. Abskharon, R. *et al.* Cryo-EM structure of RNA-induced tau fibrils reveals a small C-terminal core that may nucleate fibril formation. *Proc. Natl. Acad. Sci. U. S. A.* **119**, e2119952119 (2022).
5. Rupert, J., Monti, M., Zacco, E. & Tartaglia, G. G. RNA sequestration driven by amyloid formation: the alpha synuclein case. *Nucleic Acids Res.* **51**, 11466–11478 (2023).
6. Matsuo, K. *et al.* RNA G-quadruplexes form scaffolds that promote neuropathological α-synuclein aggregation. *Cell* **187**, 6835–6848.e20 (2024).
7. Schweighauser, M. *et al.* Structures of α-synuclein filaments from multiple system atrophy. *Nature* **585**, 464–469 (2020).
8. Garcia-Pardo, J. *et al.* Cryo-EM structure of hnRNPDL-2 fibrils, a functional amyloid associated with limb-girdle muscular dystrophy D3. *Nat. Commun.* **14**, 239 (2023).
9. Buell, A. K. *et al.* Solution conditions determine the relative importance of nucleation and growth processes in α-synuclein aggregation. *Proc. Natl. Acad. Sci. U. S. A.* **111**, 7671–7676 (2014).
10. Moran, S. D. & Zanni, M. T. How to get insight into amyloid structure and formation from

infrared spectroscopy. *J. Phys. Chem. Lett.* **5**, 1984–1993 (2014).

11. Zandomeneghi, G., Krebs, M. R. H., McCammon, M. G. & Fändrich, M. FTIR reveals structural differences between native β-sheet proteins and amyloid fibrils. *Protein Science* **13**, 3314–3321 (2004).
12. Knowles, T. P. *et al.* Role of intermolecular forces in defining material properties of protein nanofibrils. *Science* **318**, 1900–1903 (2007).
13. Ciechanover, A. & Kwon, Y. T. Proteostasis and protein degradation: Principles and diseases. *Biochimica et Biophysica Acta (BBA) - Molecular Cell Research* **1844**, 177–185 (2015).
14. Horvath, I. & Wittung-Stafshede, P. Amyloid fibers of α-synuclein catalyze chemical reactions. *ACS Chem. Neurosci.* **14**, 603–608 (2023).
15. Armaos, A., Colantoni, A., Proietti, G., Rupert, J. & Tartaglia, G. G. catRAPID omics v2.0: going deeper and wider in the prediction of protein-RNA interactions. *Nucleic Acids Res.* **49**, W72–W79 (2021).
16. Bellucci, M., Agostini, F., Masin, M. & Tartaglia, G. G. Predicting protein associations with long noncoding RNAs. *Nat. Methods* **8**, 444–445 (2011).
17. Li, B. *et al.* Cryo-EM of full-length α-synuclein reveals fibril polymorphs with a common structural kernel. *Nat. Commun.* **9**, 3609 (2018).
18. Schenker, P. & Baici, A. Paradoxical interactions between modifiers and elastase-2: Interactions between modifiers and elastase-2. *FEBS J.* **277**, 2486–2495 (2010).
19. Cerezo, M. *et al.* The NHGRI-EBI GWAS Catalog: standards for reusability, sustainability and diversity. *Nucleic Acids Res.* **53**, D998–D1005 (2025).
20. Schneider, S. A. & Alcalay, R. N. Neuropathology of genetic synucleinopathies with parkinsonism: Review of the literature. *Mov. Disord.* **32**, 1504–1523 (2017).
21. Yoshino, H. *et al.* GCH1 mutations in dopa-responsive dystonia and Parkinson's disease. *J. Neurol.* **265**, 1860–1870 (2018).

22. Shi, M.-M., Shi, C.-H. & Xu, Y.-M. Rab GTPases: The key players in the molecular pathway of Parkinson's disease. *Front. Cell. Neurosci.* **11**, 81 (2017).
23. Amick, J., Tharkeshwar, A. K., Amaya, C. & Ferguson, S. M. WDR41 supports lysosomal response to changes in amino acid availability. *Mol. Biol. Cell* **29**, 2213–2227 (2018).
24. Liu, J. & Dalamaga, M. Targeting cardiolipin metabolism for Parkinson's disease therapy. *Metabol. Open* **24**, 100327 (2024).
25. Shanbhag, N. M. *et al.* An acetylcholine M1 receptor-positive allosteric modulator (TAK-071) in Parkinson disease with cognitive impairment: A phase 2 randomized clinical trial. *JAMA Neurol.* **82**, 152–159 (2025).
26. Lorenzo-Betancor, O. *et al.* Novel compound heterozygous FBXO7 mutations in a family with early onset Parkinson's disease. *Parkinsonism Relat. Disord.* **80**, 142–147 (2020).
27. Stott, S. R. *et al.* Loss of FBXO7 results in a Parkinson's-like dopaminergic degeneration via an RPL23-MDM2-TP53 pathway. *J. Pathol.* **249**, 241–254 (2019).
28. Buneeva, O. & Medvedev, A. Ubiquitin carboxyl-terminal hydrolase L1 and its role in Parkinson's disease. *Int. J. Mol. Sci.* **25**, 1303 (2024).
29. Ayuso, P. *et al.* An association study between Heme oxygenase-1 genetic variants and Parkinson's disease. *Front. Cell. Neurosci.* **8**, 298 (2014).
30. Cressatti, M. *et al.* Glial HMOX1 expression promotes central and peripheral α-synuclein dysregulation and pathogenicity in parkinsonian mice. *Glia* **67**, 1730–1744 (2019).
31. Morelli, C. *et al.* RNA modulates hnRNPA1A amyloid formation mediated by biomolecular condensates. *Nat. Chem.* **16**, 1052–1061 (2024).
32. Intze, A. *et al.* Effect of RNA on the supramolecular architecture of α-synuclein fibrils. *Biophys. J.* **124**, 2005–2019 (2025).
33. Xu, C. K. *et al.* α-Synuclein oligomers form by secondary nucleation. *Nat. Commun.* **15**, 7083 (2024).
34. Kumari, P. *et al.* Structural insights into α-synuclein monomer-fibril interactions. *Proc. Natl.*

Acad. Sci. U. S. A. **118**, (2021).

35. Horvath, I., Welte, H., Schmit, J. D., Kovermann, M. & Wittung-Stafshede, P. Distinct growth regimes of α-synuclein amyloid elongation. *Biophys. J.* **122**, 2556–2563 (2023).
36. Schmit, J. D. Kinetic theory of amyloid fibril templating. *J. Chem. Phys.* **138**, 185102 (2013).
37. Tyedmers, J., Mogk, A. & Bukau, B. Cellular strategies for controlling protein aggregation. *Nat. Rev. Mol. Cell Biol.* **11**, 777–788 (2010).
38. Yang, Y. *et al.* Structures of α-synuclein filaments from human brains with Lewy pathology. *Nature* **610**, 791–795 (2022).
39. Langmead, B. & Salzberg, S. L. Fast gapped-read alignment with Bowtie 2. *Nat. Methods* **9**, 357–359 (2012).
40. Dobin, A. *et al.* STAR: ultrafast universal RNA-seq aligner. *Bioinformatics* **29**, 15–21 (2013).
41. Li, H. *et al.* The Sequence Alignment/Map format and SAMtools. *Bioinformatics* **25**, 2078–2079 (2009).
42. Pertea, M. *et al.* StringTie enables improved reconstruction of a transcriptome from RNA-seq reads. *Nat. Biotechnol.* **33**, 290–295 (2015).
43. Quinlan, A. R. & Hall, I. M. BEDTools: a flexible suite of utilities for comparing genomic features. *Bioinformatics* **26**, 841–842 (2010).
44. Pertea, G. & Pertea, M. GFF utilities: GffRead and GffCompare. *F1000Res.* **9**, 304 (2020).
45. Patro, R., Duggal, G., Love, M. I., Irizarry, R. A. & Kingsford, C. Salmon provides fast and bias-aware quantification of transcript expression. *Nat. Methods* **14**, 417–419 (2017).
46. Soneson, C., Love, M. I. & Robinson, M. D. Differential analyses for RNA-seq: transcript-level estimates improve gene-level inferences. *F1000Res.* **4**, 1521 (2015).
47. Pimentel, H., Bray, N. L., Puente, S., Melsted, P. & Pachter, L. Differential analysis of RNA-seq incorporating quantification uncertainty. *Nat. Methods* **14**, 687–690 (2017).
48. Harder, E. *et al.* OPLS3: A force field providing broad coverage of drug-like small molecules and proteins. *J. Chem. Theory Comput.* **12**, 281–296 (2016).

49. Halgren, T. A. *et al.* Glide: a new approach for rapid, accurate docking and scoring. 2. Enrichment factors in database screening. *J. Med. Chem.* **47**, 1750–1759 (2004).
50. Friesner, R. A. *et al.* Extra precision glide: docking and scoring incorporating a model of hydrophobic enclosure for protein-ligand complexes. *J. Med. Chem.* **49**, 6177–6196 (2006).
51. Sherman, W., Day, T., Jacobson, M. P., Friesner, R. A. & Farid, R. Novel procedure for modeling ligand/receptor induced fit effects. *J. Med. Chem.* **49**, 534–553 (2006).
52. Sherman, W., Beard, H. S. & Farid, R. Use of an induced fit receptor structure in virtual screening. *Chem. Biol. Drug Des.* **67**, 83–84 (2006).

Figures

Figure 1. RNA modulates seeded aS aggregation kinetics in a seed-dependent manner. Seeded aggregation assays performed under quiescent conditions using aS seeds generated in the absence (protein^{only} seeds) or presence of RNA (protein^{RNA} seeds, see **Materials and Methods**). (*A*) Proteostat™ fluorescence of 50 μM aS during seeded aggregation at varying seed concentrations, in the presence or absence of RNA. All conditions show exponential increases without detectable lag phase (*B*) Initial elongation rates extracted from the early linear phase of aggregation. At higher seed concentrations (5 μM and 10 μM), RNA significantly enhances elongation ($p < 0.0001$, $N = 8$, two-way Student's *t*-test), whereas at 1 μM protein^{only} seeds elongate faster in the absence of RNA ($p < 10^{-5}$, $N = 8$).

Figure 2. RNA modulates aS fibril elongation in a seed-dependent manner. (*A*) Aggregation rates of protein^{only} seeds at varying seed concentrations, in the presence or absence of RNA. RNA slows the rate at lower seed concentration but accelerates it at seed concentration above 5 μM (*B*) Aggregation rates of protein^{RNA} seeds under the same conditions. The rate remains consistently low without RNA and shows little change at increasing seed concentrations, indicating the RNA is crucial in the aggregation and replication of protein^{RNA} seeds.

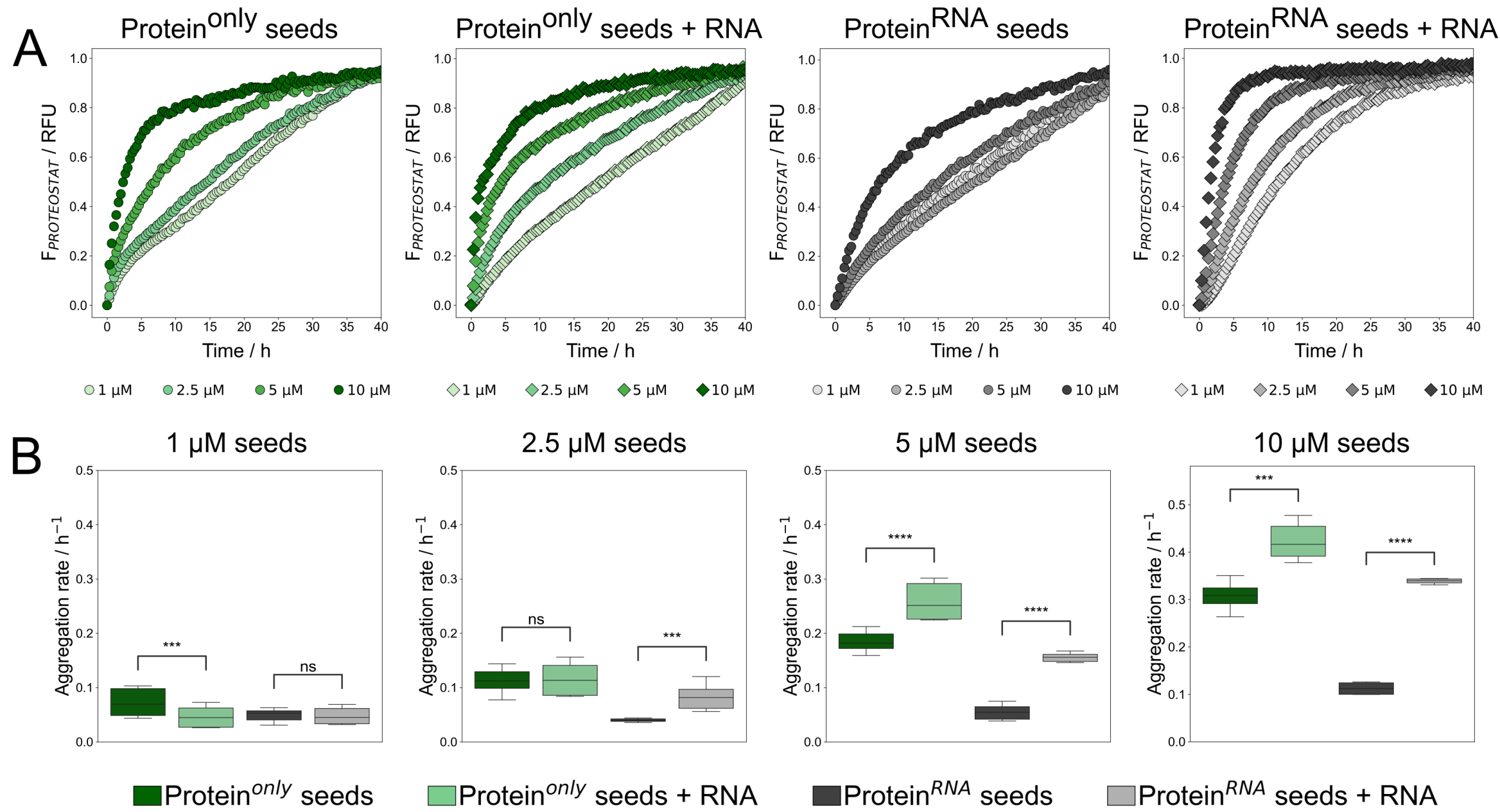
Figure 3. RNA alters structural properties of aS fibrils. (*A*) Cross-β peak positions ($\omega_{cross\text{-}\beta}$) from FTIR spectra of fibrils from protein^{only} (green) and protein^{RNA} (grey) seeds. (*B*) Distribution of $\omega_{cross\text{-}\beta}$ values from micro-FTIR spectra recorded with a focal plane array detector. Protein^{RNA} fibrils show a higher proportion of the peak at 1625.8 cm^{-1} compared to protein^{only} fibrils and a shift in the $\omega_{cross\text{-}\beta}$ of the upper peak towards lower frequencies. *(C)* Representative AFM maps of protein^{only} and protein^{RNA} fibrils.

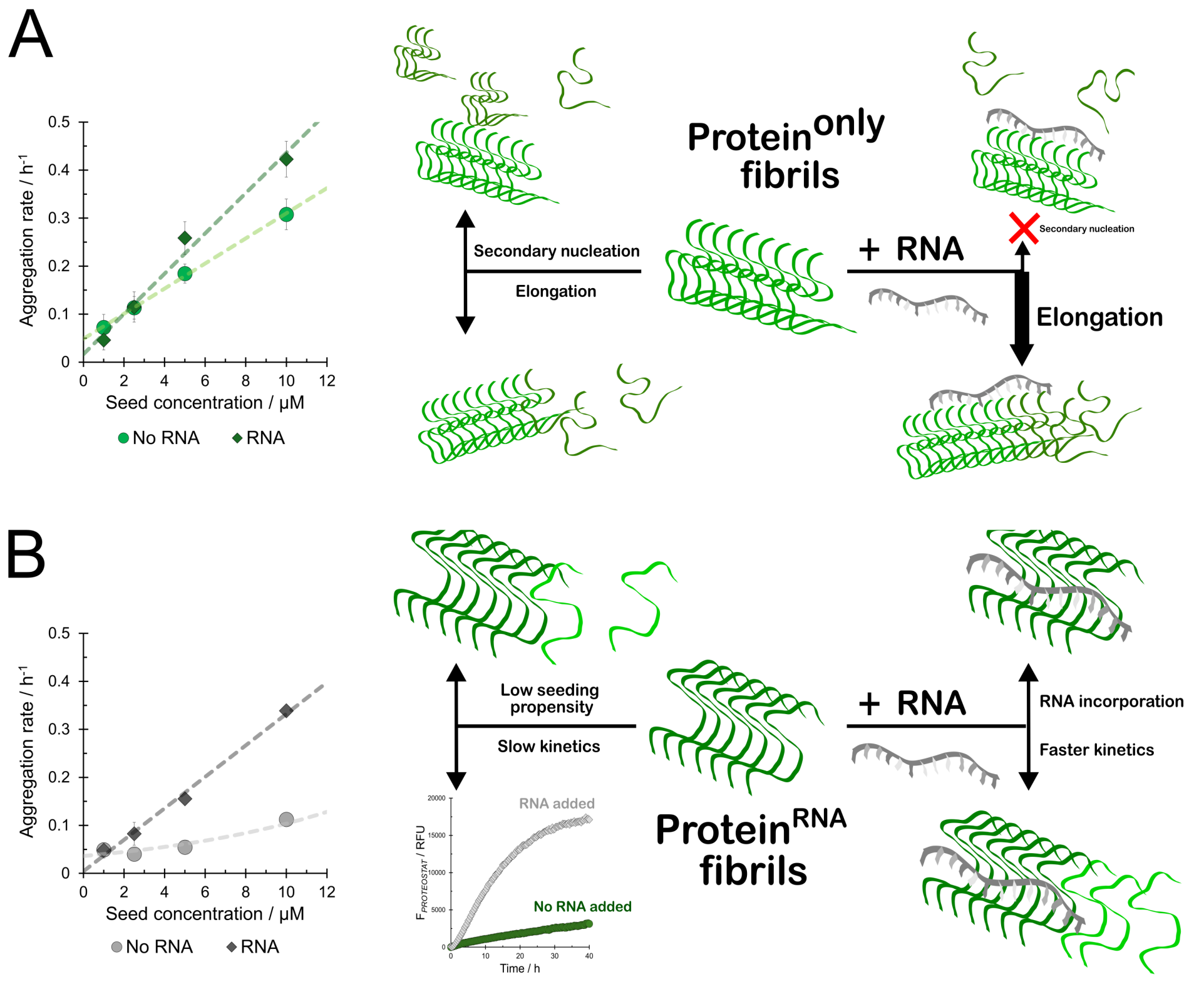
Figure 4. RNA reduces proteinase K–mediated degradation of aS fibrils. (*A*) Real-time Proteostat™ fluorescence of protein^{only} and protein^{RNA} fibrils at increasing RNA concentrations (0 – 500 ng/μL). Higher RNA levels slow fluorescence decay in a concentration-dependent manner. (*B*) Quantified degradation rates show RNA significantly decreases the degradation rate ($p < 10^{-10}$, N = 30 (protein^{only} seeds), N = 24 (protein^{RNA} seeds), two-way Student t-test), while RNase A treatment significantly increases the rate of degradation for protein^{only} fibrils ($p < 10^{-5}$, N = 30, two-way Student t-test). (*C*) Summary schematic illustrating RNA-dependent inhibition of fibril degradation.

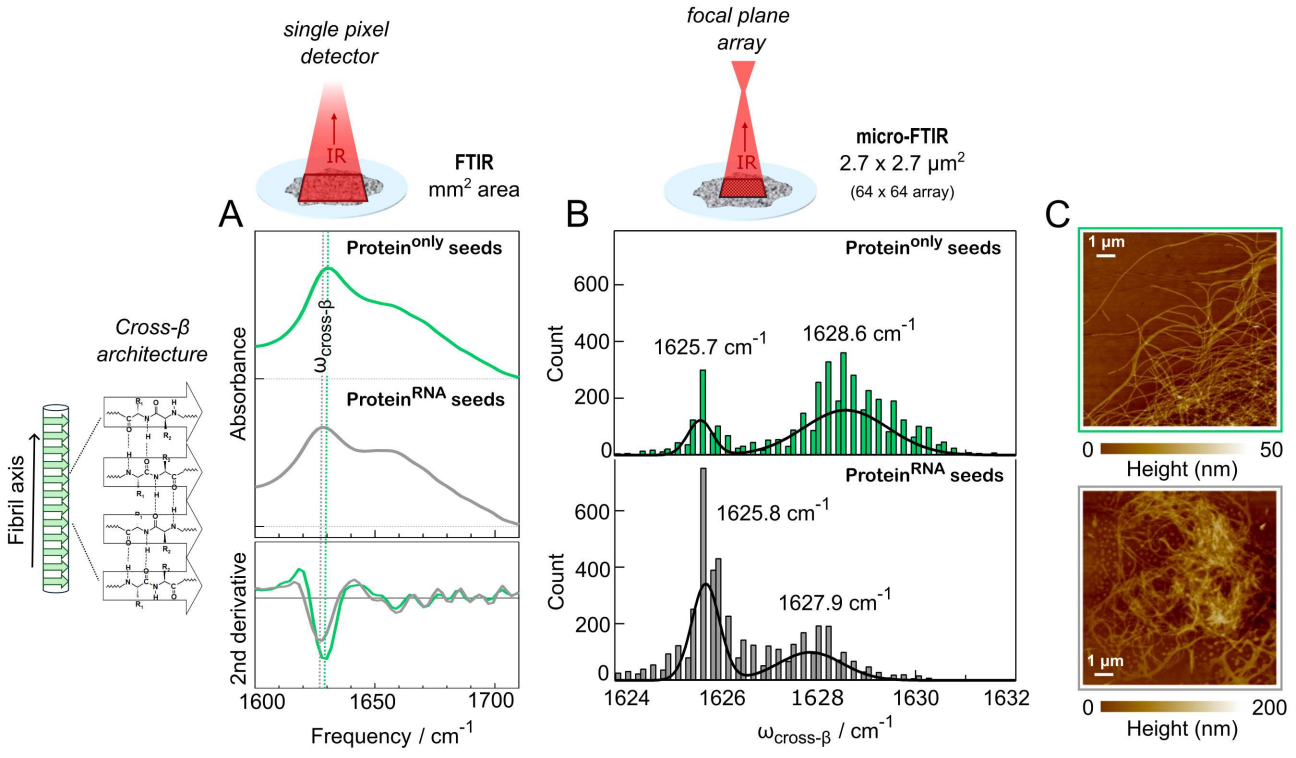
Figure 5. RNA inhibits catalytic activity of aS fibrils. (***A***) Catalytic site linked to H50 (red) in the rod 1a polymorph of aS (PDB 6CU7), located in a region predicted to bind RNA (T44–T59, green; *cat*RAPID score > 0.5, **Supp. Fig. 4**). (*B*) Initial velocities of esterase (pNPA) and phosphatase (pNPP) activity decrease with increasing RNA concentration. Logistic fits estimate apparent RNA-

binding affinities ($K_{0.5}$ = 680 ng/µL for pNPA, 602 ng/µL for pNPP). (*C*) Fibrils grown from RNA- or heparin-treated seeds show minimal catalytic activity, consistent with RNA-dependent structural alteration of the catalytic site.

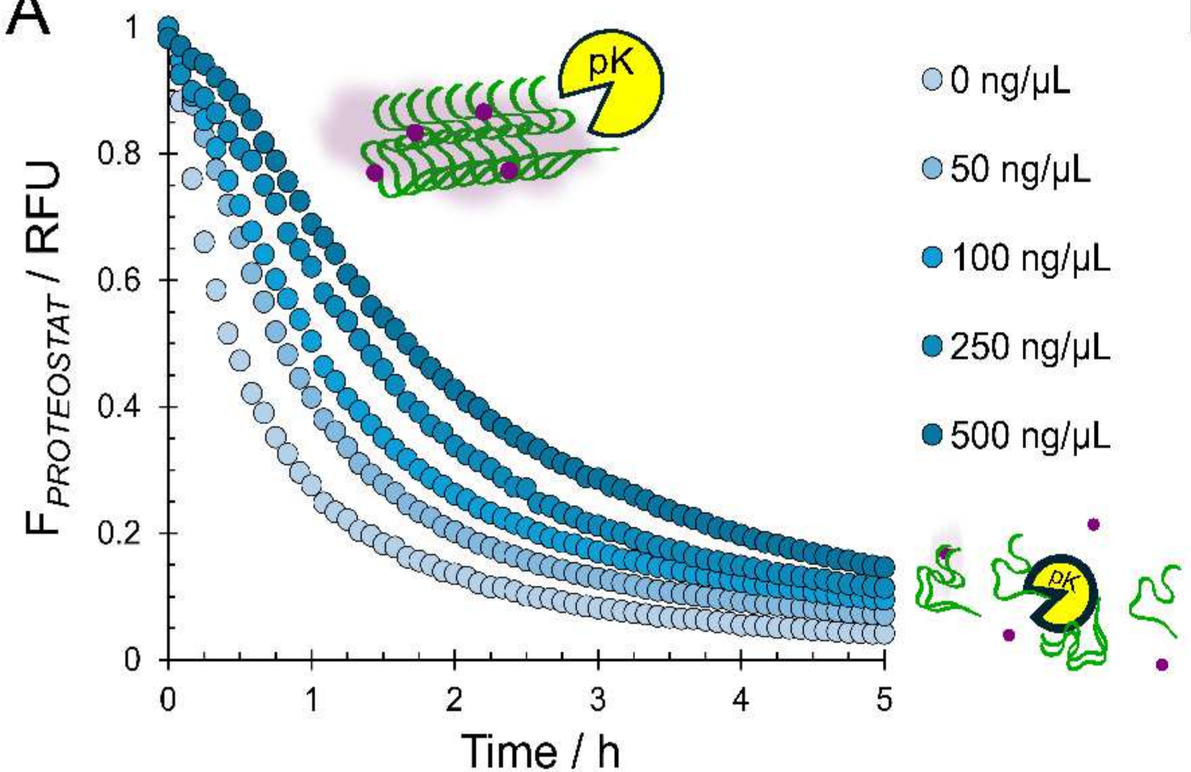
Figure 6. aS fibrils preferentially bind uridine-rich RNA. *(A) Hexamer enrichment analysis of RNA extracted from proteinRNA fibrils versus abundance-matched control RNAs. Left: Volcano plot of log(OR) versus –log_{10}(adjusted p-value), highlighting the 10 most enriched (red) and 10 most depleted (blue) hexamers. Right: Table with sequence, OR, p-value, and adjusted p-value. (B,C)* Docking of uridine monophosphate into the central cavity of the MSA patient–derived aS fibril (PDB 6XYP) shows planar orientation between layers. Both RNA and DNA nucleotides can occupy the cavity, with pyrimidines preferentially accommodated.


A
Protein^only seeds
Protein^only seeds + RNA
Protein^RNA seeds
Protein^RNA seeds + RNA
F_PROTEOSTAT / RFU
Time / h
1 µM
2.5 µM
5 µM
10 µM
B
1 µM seeds
2.5 µM seeds
5 µM seeds
10 µM seeds
Aggregation rate / h^−1
***
ns
****
Protein^only seeds
Protein^only seeds + RNA
Protein^RNA seeds
Protein^RNA seeds + RNA

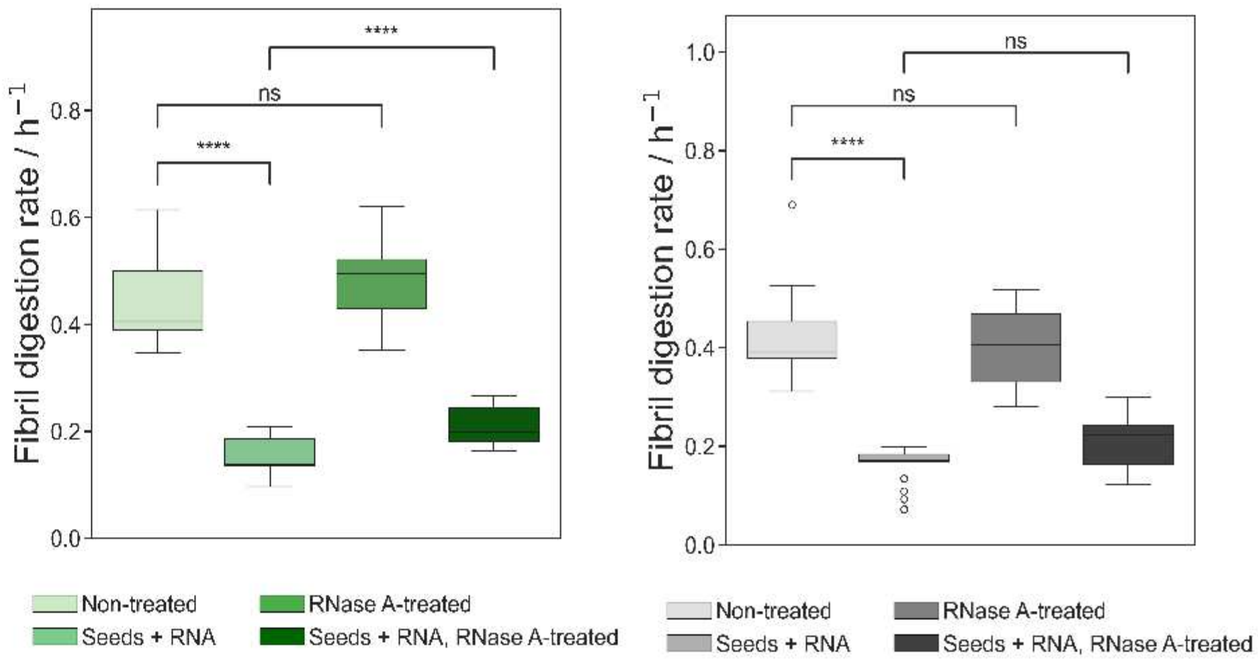

A
Aggregation rate / h-1
0.5
0.4
0.3
0.2
0.1
0
0
2
4
6
8
10
12
Seed concentration / μM
No RNA
RNA
Protein only fibrils
Secondary nucleation
Elongation
+ RNA
Secondary nucleation
Elongation
B
Aggregation rate / h-1
0.5
0.4
0.3
0.2
0.1
0
0
2
4
6
8
10
12
Seed concentration / μM
No RNA
RNA
Low seeding propensity
Slow kinetics
+ RNA
RNA incorporation
Faster kinetics
RNA added
No RNA added
F PROTEOSTAT / RFU
20000
15000
10000
5000
0
0
10
20
30
40
Time / h
Protein RNA fibrils


single pixel detector
IR
FTIR
mm² area
focal plane array
IR
micro-FTIR
2.7 x 2.7 µm²
(64 x 64 array)
A
B
C
Cross-β architecture
Fibril axis
Protein^only seeds
Protein^RNA seeds
Absorbance
ω cross-β
2nd derivative
1600
1650
1700
Frequency / cm⁻¹
Count
1625.7 cm⁻¹
1628.6 cm⁻¹
1625.8 cm⁻¹
1627.9 cm⁻¹
1624
1626
1628
1630
1632
ω cross-β / cm⁻¹
1 µm
0
50
Height (nm)
200

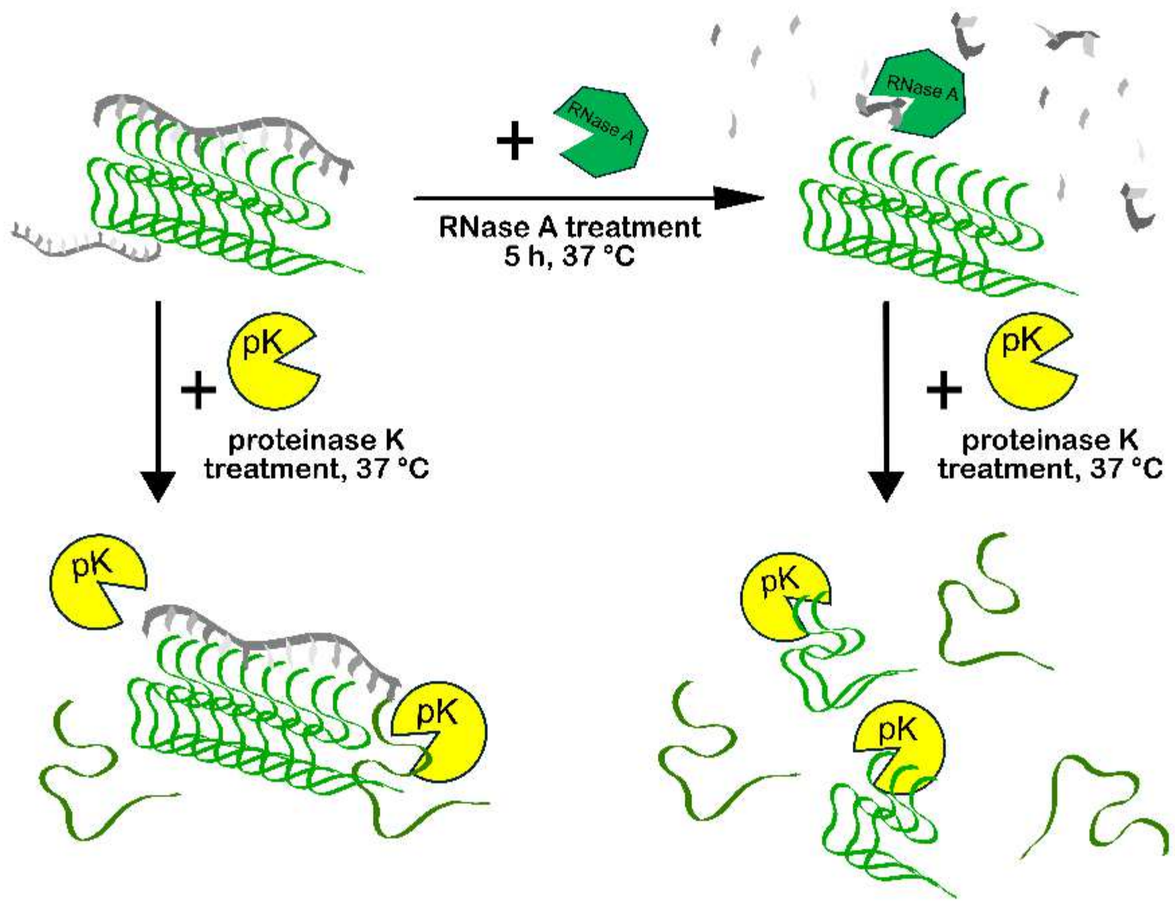
A

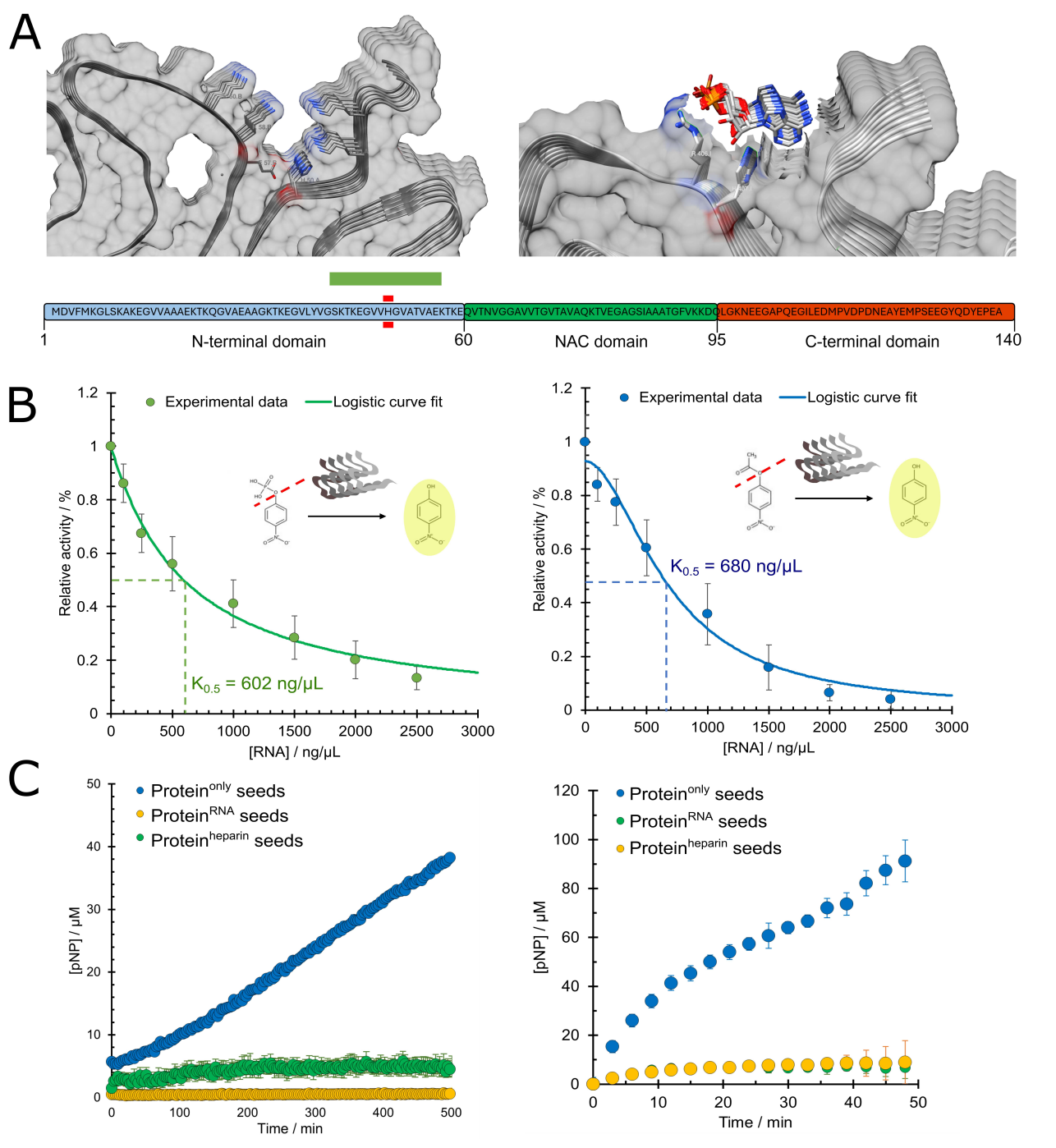

$F_{PROTEOSTAT}$ / RFU
Time / h
0 ng/µL
50 ng/µL
100 ng/µL
250 ng/µL
500 ng/µL
pK

B

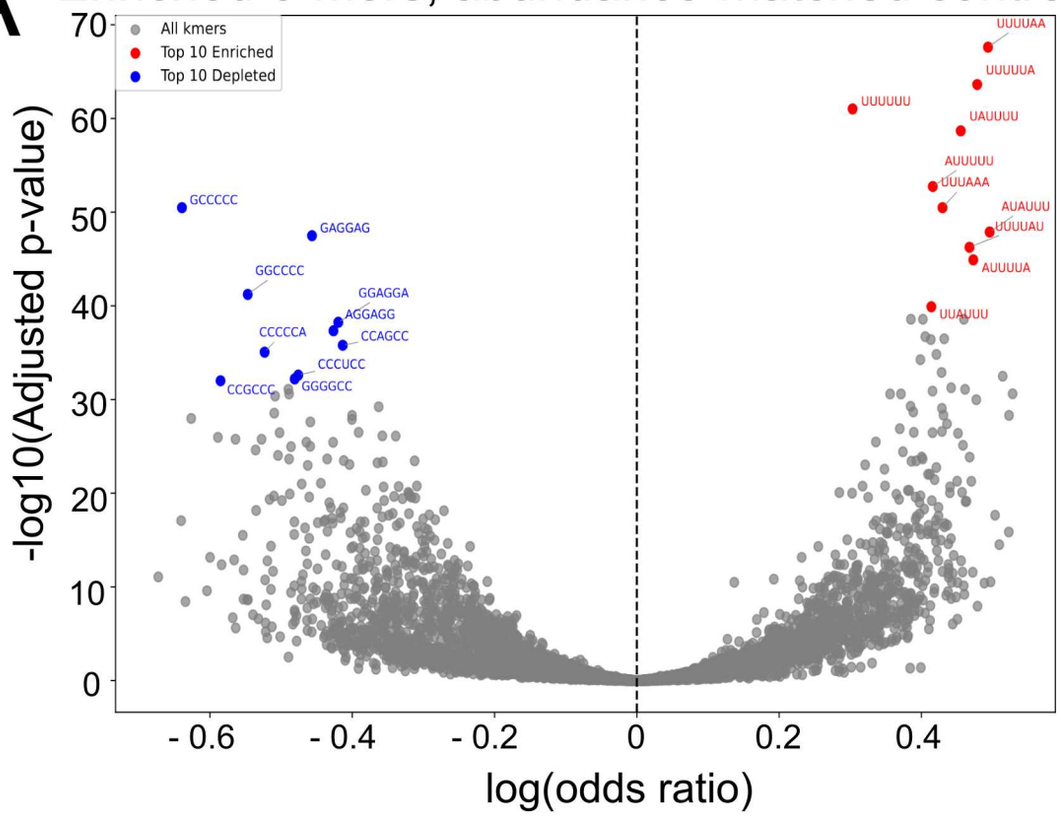

Fibril digestion rate / h^{-1}
ns
****
Non-treated
Seeds + RNA
RNase A-treated
Seeds + RNA, RNase A-treated

C


RNase A
RNase A treatment
5 h, 37 °C
pK
proteinase K
treatment, 37 °C

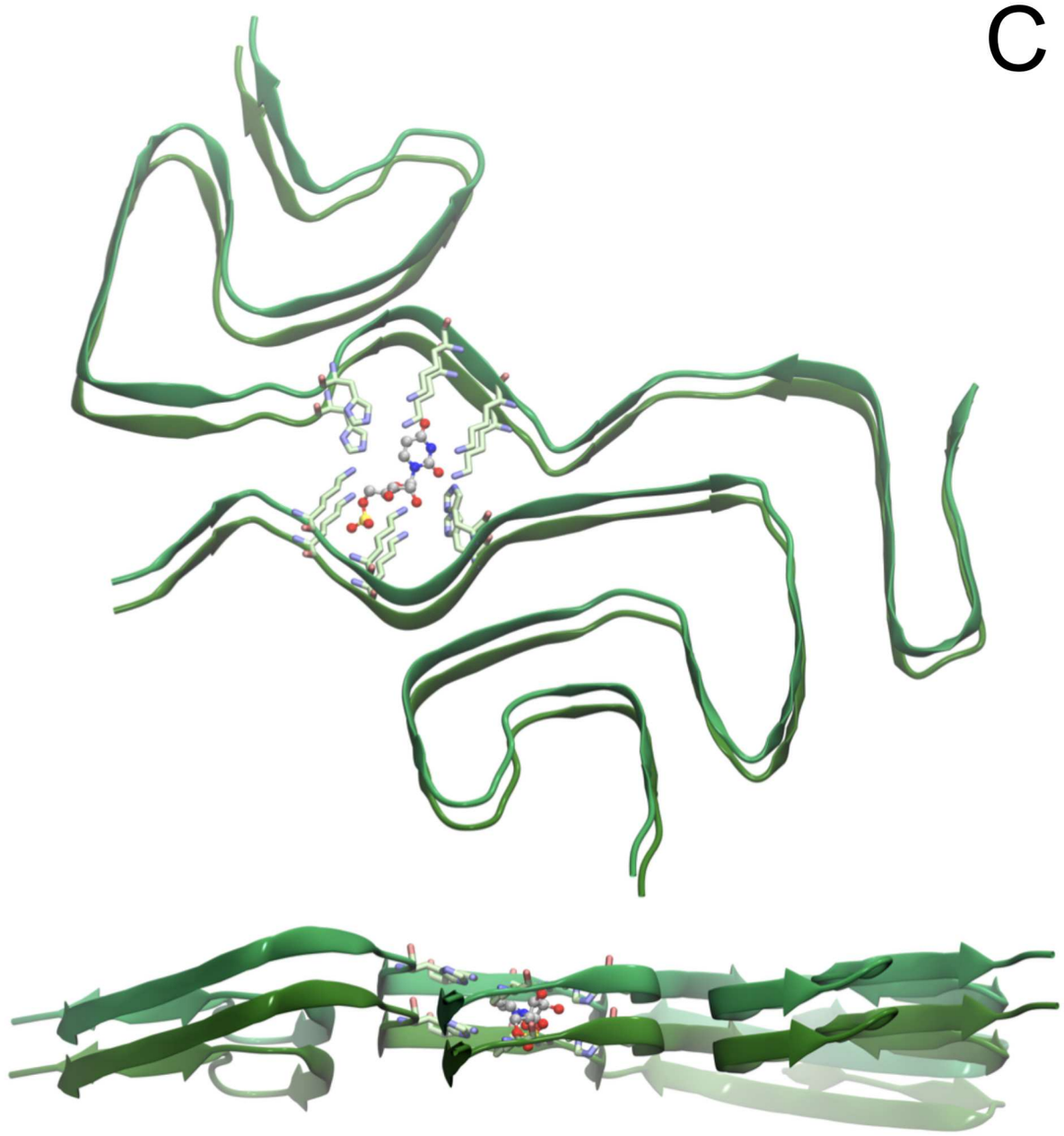

A
MDVFMKGLSKAKEGVVAAAEKTKQGVAEAAGKTKEGVLYVGSKTKEGVVHGVATVAEKTKE
QVTNVGGAVVTGVTAVAQKTVEGAGSIAAATGFVKKDQLGKNEEGAPQEGILEDMPVDPDNEAYEMPSEEGYQDYEPEA
1
N-terminal domain
60
NAC domain
95
C-terminal domain
140
B
Experimental data
Logistic curve fit
Relative activity / %
[RNA] / ng/µL
K0.5 = 602 ng/µL
Experimental data
Logistic curve fit
Relative activity / %
[RNA] / ng/µL
K0.5 = 680 ng/µL
C
Protein only seeds
Protein RNA seeds
Protein heparin seeds
[pNP] / µM
Time / min
Protein only seeds
Protein RNA seeds
Protein heparin seeds
[pNP] / µM
Time / min

A

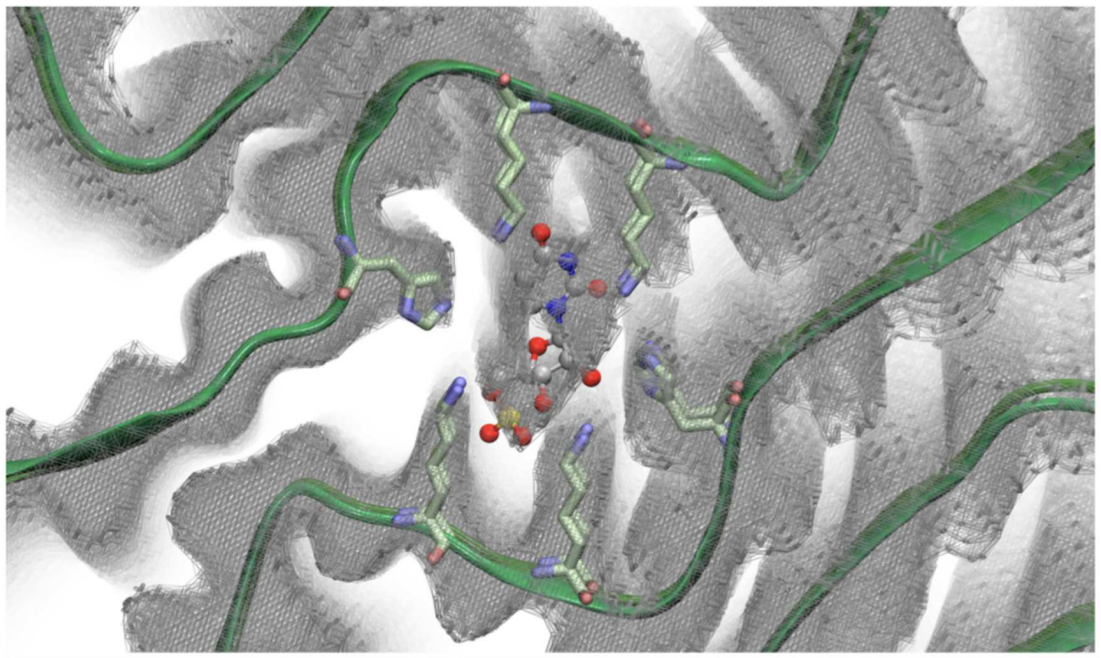


Top 10 depleted motifs					Top 10 enriched motifs				
Rank	RNA motif	Odds Ratio	p-value	Adjusted p-value	Rank	RNA motif	Odds Ratio	p-value	Adjusted p-value
1	GCCCCC	0.527622	5.43E-54	3.31E-51	1	UUUUAA	1.63839	5.89E-72	2.41E-68
2	GAGGAG	0.633447	7.15E-51	3.25E-48	2	UUUUUA	1.613654	1.16E-67	2.37E-64
3	GGCCCC	0.578742	1.74E-44	5.93E-42	3	UUUUUU	1.354367	7.02E-65	9.58E-62
4	GGAGGA	0.657274	2.36E-41	5.69E-39	4	UAUUUU	1.576748	2.05E-62	2.1E-59
5	AGGAGG	0.652858	2.02E-40	4.59E-38	5	AUUUUU	1.516007	2.2E-56	1.8E-53
6	CCAGCC	0.661376	8.54E-39	1.59E-36	6	UUUAAA	1.536764	5.65E-54	3.31E-51
7	CCCCCA	0.592632	4.94E-38	8.8E-36	7	AUAUUU	1.642121	2.56E-51	1.31E-48
8	CCCUCC	0.621339	1.63E-35	2.48E-33	8	UUUUAU	1.596183	1.37E-49	5.62E-47
9	GGGGCC	0.618216	4.41E-35	6.23E-33	9	AUUUUA	1.604785	3.28E-48	1.22E-45
10	CCGCCC	0.557033	7.27E-35	9.93E-33	10	UUAUUU	1.512878	3.99E-43	1.26E-40

B



C



Ligand	Atom count	Glide Score	Predicted contacts	Putative clashes
rU	33	-7.904	8	1
dT	35	-6.993	7	3
rC	34	-6.921	6	2
dC	33	-6.012	5	2
rG	37	-4.155	4	3
dG	36	-3.460	3	4
rA	36	-3.289	4	4
dA	35	-2.677	3	5

Supplementary Files

This is a list of supplementary files associated with this preprint. Click to download.

- SupplementaryTable1.docx
- SupplementaryTable2new.xlsx
- RupertSupplementaryNSMB.pdf